ACS APPLIED MATERIALS & INTERFACES

Research Article

www.acsami.org

CNTs in Situ Attached to α-Fe_2O_3 Submicron Spheres for Enhancing Lithium Storage Capacity

Guo Gao,*[,†] Qiang Zhang,[‡] Xin-Bing Cheng,[‡] Peiyu Qiu,[†] Rongjin Sun,[†] Ting Yin,[†] and Daxiang Cui*[,†]

[†]Institute of Nano Biomedicine and Engineering, Department of Instrument Science and Technology, Key Laboratory for Thin Film and Microfabrication Technology of Ministry of Education, School of Electronic Information and Electrical Engineering, Shanghai Jiao Tong University, Shanghai 200240, China

[‡]Beijing Key Laboratory of Green Chemical Reaction Engineering and Technology, Department of Chemical Engineering, Tsinghua University, Beijing 100084, China

Supporting Information

ABSTRACT: In this work, we developed a facile hydrothermal method for synthesis of hybrid α-Fe_2O_3–carbon nanotubes (CNTs) architectures (α-Fe_2O_3–CNTs-1 and α-Fe_2O_3–CNTs-2). The CNTs are in situ attached to the α-Fe_2O_3 submicron spheres and form three-dimensional network robust architectures. The increase in the amount of CNTs in the network α-Fe_2O_3–CNTs architectures will significantly enhance the cycling and rate performance, as the flexible and robust CNTs could ensure the fast electron transport pathways, enhance the electronic conductivity, and improve the structural stability of the electrode. As for pure α-Fe_2O_3 submicron spheres, the capacity decreased significantly and retained at 377.4 mAh g^{-1} after 11 cycles, and the capacity has a slightly increasing trend at the following cycling. In contrast, the network α-Fe_2O_3–CNTs-2 electrode shows the most remarkable performance. At the 60th cycle, the capacity of network α-Fe_2O_3–CNTs-2 (764.5 mAh g^{-1}) is 1.78 times than that of α-Fe_2O_3 submicron spheres (428.3 mAh g^{-1}). The long-term cycling performance (1000 cycles) of samples at a high current density of 5 C showed that the capacity of α-Fe_2O_3 submicron spheres fade to ~37.3 mAh g^{-1} at the 400th cycle and gradually increased to ~116.7 mAh g^{-1} at the 1000th cycle. The capacity of network α-Fe_2O_3–CNTs-2 maintained at ~220.2 mAh g^{-1} before the 400th cycle, arrived at ~326.5 mAh g^{-1} in the 615th, cycle and retained this value until 1000th cycle. The network α-Fe_2O_3–CNTs-2 composite could significantly enhance the cycling and rate performance than pure α-Fe_2O_3 submicron spheres composite.

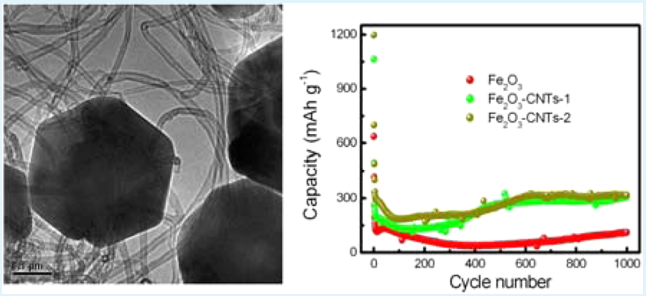

KEYWORDS: *α-Fe_2O_3, submicron spheres, CNTs, composites, hydrothermal, LIBs*

1. INTRODUCTION

Recently, the consumption of fossil fuels increases significantly due to the rapid scientific and technological developments. Exploring novel clean energy to satisfy our future energy demand is becoming an emergency strategic topic.[1−6] Rechargeable lithium-ion batteries (LIBs) are deemed to be the most promising candidate as the clean resources in the near future. LIBs are typically consisted by a lithium metal oxide (e.g., $LiCoO_2$) in the cathode, a carbon-based material (e.g., graphite) in the anode and together with electrolyte-filled porous membrane separator.[7] During the charge/discharge, lithium ions flow between the anode and the cathode, and the electrons move to the cathode and combine with lithium ions, enabling the storage/conversion of chemical energy and electrical energy.[8−10]

Recent advances in nanomaterials open up new opportunities to obtain different architectures with the desired shapes and compositions as electrode materials for LIBs to further improving their electrochemical performance.[11−16] These special properties make nanostructured materials ideal candidates for the anodes of LIBs. To date, although great progress has been made in the area of LIBs,[17−20] economical implementation of LIBs on a global scale still requires great advances in both advanced electrode materials and devices to decrease the production cost and increase the electrochemical performance. Recently, hematite (Fe_2O_3) was considered a promising anode material for LIBs because of its high theoretical capacity (1005 mAh g^{-1}), low cost, and natural abundance.[21−23] However, the cycling performance and rate capability of Fe_2O_3 electrodes still need further improvements due to the large volume change and low electronic conductivity of Fe_2O_3 during the lithiation and delithiation process. Our previous studies show that the cycling performance and rate capability of iron oxides can be significantly improved with the addition of carbon nanotubes (CNTs).[24−26] On the other hand, we have demonstrated that network nanocomposites of

Received: September 13, 2014
Accepted: December 9, 2014
Published: December 9, 2014

CNTs and metal oxides facilitate the charge transport and maintain the structural integrity, leading to high capacity, high rate, and excellent cycling performance.[27] Recently, Li et al. also reported that three-dimensional network structured α-Fe_2O_3 exhibited high electrochemical performance as the anode materials of LIBs.[28] Although considerable advances have been made in the synthesis of network architectures, there is still much room to progress, especially for the construction of well-defined three-dimensional network architectures for anode materials of LIBs.

In this contribution, we developed a one-pot hydrothermal method for the controllable synthesis of network α-Fe_2O_3–CNTs hybrid composites. The formation process is shown in Scheme 1. This method employed cetyltrimethylammonium bromide (CTAB) and F127 as soft template, the oxidized CNTs as the frameworks, and $FeCl_3{\cdot}6H_2O$ as iron resources. With the addition of Na_2CO_3 solution, CO_3^{2-} will react with Fe^{3+} ions and produce numerous nuclei of Fe^{3+} precipitates. To minimize the energy of reaction system, these nuclei of Fe^{3+} precipitates tend to aggregate and form irregular assemblies. However, the agglomeration behavior can be effectively controlled by the geometric constrains of long alkyl chain CTAB and multiactive sites F127. Therefore, these nuclei of Fe^{3+} precipitates are well dispersed. When the oxidized CNTs were added in the solution, the surface of CNTs will be homogeneously aggregated by the nuclei of Fe^{3+} precipitates due to the oxidized CNTs containing rich oxygen functionalities, which can act as the active sites for the agglomeration of Fe^{3+} precipitates. During the hydrothermal process, Fe^{3+} precipitates are decomposed into the α-Fe_2O_3 particles, and one-dimensional CNTs are in situ attached to the α-Fe_2O_3 particles. The tangling effect of CNTs and the dispersive effect of surfactant promote the formation of well-defined network α-Fe_2O_3–CNTs composites. The main advantages of the current synthetic method are (1) the introduction of oxidized CNTs may improve the electronic conductivity of electrode, facilitate charge transfer between the electrode and electrolyte, and trap extra Li^+ via the inner holes and defects of the oxidized CNTs in the discharge process; (2) the flexible and robust CNT backbone can tolerate the large volume variation and inhibit the severe particles aggregation during the repeated charge/discharge cycling process; and (3) the CNTs are in situ attached to the α-Fe_2O_3 particles, which will induce the disassembly of the α-Fe_2O_3 submicron particles from an integrated one into the assemblies composed of numerous small-sized particles (5–10 nm). This evolution will be helpful for further improving the electrochemical performance.

Scheme 1. Formation Process of Hybrid Network α-Fe_2O_3–CNTs Architectures

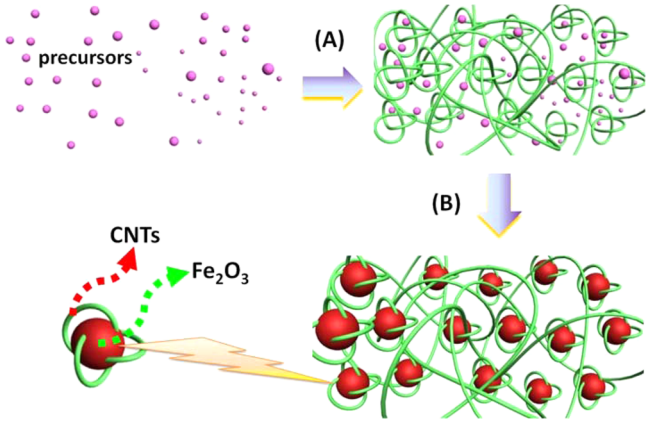

2. EXPERIMENTAL SECTION

2.1. Synthesis and Oxidation of Multi-walled CNTs. The multi-walled CNTs were synthesized according to our previous procedure.[29] This procedure involves the design of catalyst, the agglomerate control, and the fluidization hydrodynamic process. The synthesized CNTs were 20–40 nm in diameter and 30–100 μm in length. After the CNTs were fabricated, they were oxidized by the strong mixed acid solution. Typically, 1 g of CNTs was added into a Teflon-lined stainless autoclave, then 10 mL of HNO_3 and 30 mL of H_2SO_4 were added. The mixture was stirred for about 20 min. After that, the stainless autoclave was screwed down and heated at 80 °C for 20 min. Then, the oxidized CNTs were cooled to room temperature, filtered, washed with deionized water, and dried in a freeze-drying apparatus for 24 h. The morphologies of CNTs and the oxidized CNTs are shown in Figure S1 (Supporting Information).

2.2. Synthesis of Network α-Fe_2O_3–CNTs Architectures. In a typical procedure, 0.2 M $FeCl_3{\cdot}6H_2O$ solution was mixed with 0.1 M cetyltrimethylammonium bromide (CTAB) and 0.05 g of F127 in a volume ratio of 1:1. Then, 25 mL of Na_2CO_3 solution (0.2 M) was gradually added. The mixture was continuously stirred for 20 min. After that, to the mixed solution was added different amounts of oxidized CNTs (0, 0.02, and 0.05 g). About 10 min of ultrasonic treatment for the mixture was necessary to fully disperse the oxidized CNTs in the mixture. Then the mixture was transferred into a Teflon-lined stainless autoclave and heated to 260 °C for 10 h. After reaction, the obtained pure α-Fe_2O_3 and network α-Fe_2O_3–CNTs composites (according to the initial addition amount of CNTs (0.02 and 0.05 g), the resulting network α-Fe_2O_3–CNTs composites (abbreviated as α-Fe_2O_3–CNTs-1 and α-Fe_2O_3–CNTs-2, respectively) were filtered, washed with deionized water, and dried in a freeze-drying apparatus for 24 h.

2.3. Characterization. X-ray diffraction (XRD, Rigaku, Japan) patterns of the samples were recorded by an X-ray powder diffractometer using Cu Kα radiation (λ = 1.5418 Å). Morphologies and structures of samples were observed by scanning electron microscopy (SEM, FEI-Sirion 200) and transmission electron microscopy (TEM, JEM-2010). The magnetic behavior of the synthesized α-Fe_2O_3 particles and network α-Fe_2O_3–CNTs architectures was analyzed using a vibrating sample magnetometer (VSM, Lake Shore 736, Westerville, OH). The weight percentage of CNTs content in the network α-Fe_2O_3–CNTs architectures was determined by a thermogravimetric analyzer (Pyris 1 TGA, PerkinElmer, Waltham, MA) under air atmosphere at a heating rate of 10 °C min^{-1} from 20 to 800 °C. The particle size distribution of the α-Fe_2O_3 particles was evaluated by a nano particle analyzer (NANOS/ZEN1600, Malvern). The Raman spectrum of samples was taken by a SENTERRA R200 Raman microscope. Fourier transform infrared spectroscopy (FTIR) was carried out by a PerkinElmer Paragon-1000 spectrometer.

2.4. Electrochemical Measurements. To evaluate the electrochemical performance of the synthesized α-Fe_2O_3 particles and network α-Fe_2O_3–CNTs architectures, we used CR2025-coin type cells with the composites. The working electrode was prepared by mixing the active materials, acetylene black, and polyvinylidene fluoride (PVDF) with weight ratios of 80:10:10 in *N*-methyl-2-pyrrolidone solvent. The resulting slurry was then uniformly coated on a copper foil using a blade, and then dried at 120 °C in a vacuum oven. Coin cells were assembled in an argon-filled glovebox with the water and oxygen content less than 0.5 ppm. Pure Li foil was used as both the counter electrode and the reference electrode. The electrolyte was 1 M $LiPF_6$ in ethylene carbonate, diethyl carbonate and ethylmethyl carbonate (EC/DMC/EMC, volume ratio of 1:1:1) electrolyte. A polypropylene membrane (Celgard 2400) was used as a separator.

dx.doi.org/10.1021/am506238q | ACS Appl. Mater. Interfaces 2015, 7, 340–350

3. RESULTS AND DISCUSSION

The network α-Fe_2O_3−CNTs architectures were synthesized by a facile one-pot hydrothermal method using $FeCl_3 \cdot 6H_2O$ and multiwalls carbon nanotubes (CNTs) as raw materials. The structure and phase information on composites were confirmed by the XRD measurements, as shown in Figure S2 (Supporting Information). Without the addition of CNTs, pure α-Fe_2O_3 composites can be obtained. All of the diffraction peaks can be well indexed to the hematite α-Fe_2O_3 structure (JCPDS No. 33-664) with lattice constants a = 0.5036 and c = 1.375. The sharp diffraction peaks show that the α-Fe_2O_3 composites have a relatively high crystallinity. With the addition of CNTs (0.02 g), the resulting composites are composed of hematite α-Fe_2O_3 and carbon nanotubes. The broad peak at 2θ = 25.6° can be assigned to the (002) plane of CNTs. With the further increase in the amount of CNTs (0.05 g), the peak becomes increasingly evident. On the other hand, it can be seen that the peak intensity of α-Fe_2O_3 has a descending trend with the increase of CNTs. This reason may be attributed to the increase of CNTs in the hydrothermal system influences the crystallinity of α-Fe_2O_3. As for iron oxide nanomaterials, it is widely accepted the crystallinity was related to their magnetic behavior. Generally, the high crystallinity will lead to the high saturation magnetization. To monitor the crystallinity evolution of network α-Fe_2O_3−CNTs architectures, we evaluated the resulting composites by a vibrating sample magnetometer (VSM) analyzer at room temperature, as shown in Figure S3 (Supporting Information). It can be seen that pure α-Fe_2O_3 composite has a high saturation magnetization (0.61 emu/g), remanent magnetization (0.22 emu/g), and coercivity (1027.3 Oe). With the addition of CNTs (0.02 g), all of the parameters have a decreasing trend. The saturation magnetization, remanent magnetization, and coercivity are found to be 0.59 emu/g, 0.20 emu/g, and 287.2 Oe, respectively. With the further increase of CNTs (0.05 g), the saturation magnetization (0.57 emu/g) and remanent magnetization (0.18 emu/g) have a continuously decreasing trend, but the coercivity presenting an increasing trend (599.2 Oe). Compared with the pure α-Fe_2O_3 composite, network α-Fe_2O_3−CNTs architectures exhibit the low saturation magnetization, remanent magnetization, and coercivity, confirming the crystallinity α-Fe_2O_3 becomes weak due to the influence of CNTs in the hydrothermal system.

Figure 1a shows the microstructure of the as-prepared pure α-Fe_2O_3 composites. It is clearly seen that the pure α-Fe_2O_3 composites are composed of small-size submicron spheres (~200 nm) and large-size submicron spheres (400−500 nm). The ratio of small-size particles and large-size particles is nearly 1:1. The α-Fe_2O_3 submicron spheres are highly dispersed and have a well-defined edge (Figure 1b). The average diameter of pure α-Fe_2O_3 composites was measured to be 537.1 nm, which was slightly larger than the real size of α-Fe_2O_3 particles because the measured size was the hydrodynamic diameter of the dynamic light scatting in solution. Figure 1c shows the morphology of the as-prepared network α-Fe_2O_3−CNTs-1 architectures. It can be seen that the α-Fe_2O_3 submicron spheres are tangled by one-dimensional CNTs. Compared with pure α-Fe_2O_3 composites (Figure 1a), the average size of α-Fe_2O_3 submicron spheres in the network α-Fe_2O_3−CNTs-1 architectures has a decreasing trend and is mainly distributed in the range of 250−350 nm. No large-size α-Fe_2O_3 particles (e.g., 500 nm) are observed in the network α-Fe_2O_3−CNTs-1

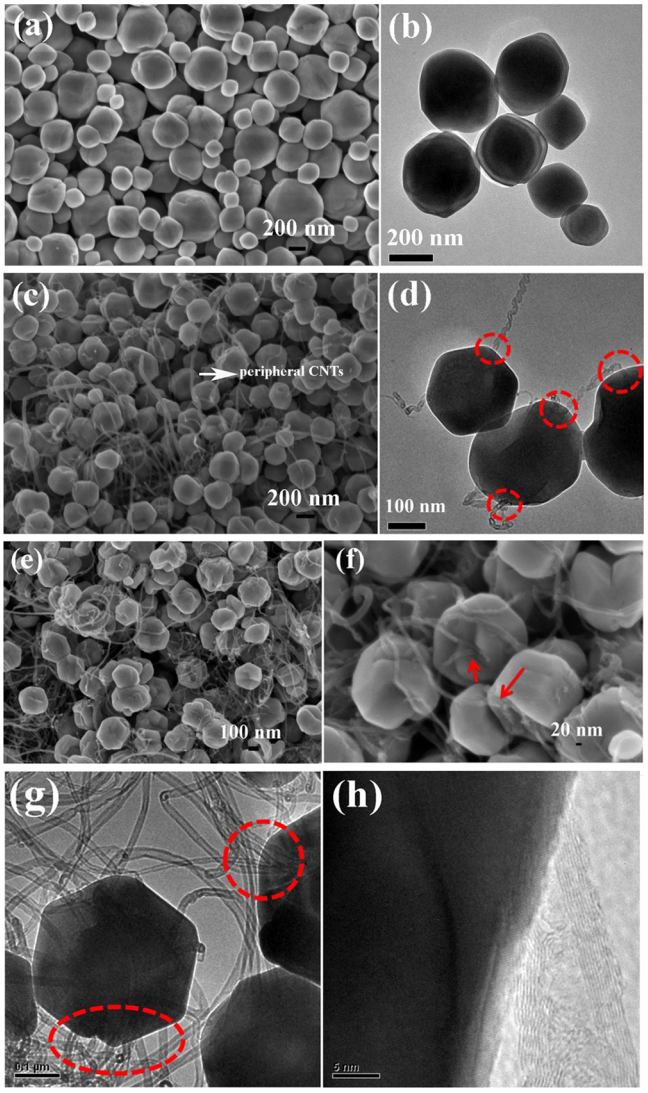

Figure 1. (a) SEM and (b) TEM images of the pure α-Fe_2O_3 composites, (c) SEM and (d) TEM images of the network α-Fe_2O_3−CNTs-1 architectures, and (e) SEM, (f) TEM and (g and h) HRTEM images of the network α-Fe_2O_3−CNTs-2 architectures.

architectures owing to the surface of oxidized CNTs having numerous oxygen-containing groups, which may have a dispersive effect for the nuclei of Fe^{3+} precipitates. Figure 1d clearly shows that some CNTs are attached in the α-Fe_2O_3 submicron spheres. Owing to the tangling effect between the attached CNTs in α-Fe_2O_3 submicron spheres and the peripheral CNTs, robust network architectures are formed. With the further increase of CNTs, α-Fe_2O_3 submicron spheres are tangled by much more CNTs, as shown in Figure 1e. On the other hand, the average size of α-Fe_2O_3 submicron spheres has a further decreasing trend, and the majority of the particles are distributed in the range of 200−250 nm. The higher magnification image in Figure 1f clearly shows that CNTs are attached in the α-Fe_2O_3 submicron spheres and entangled by the CNTs (Figure S4, Supporting Information). The diameter of the attached CNTs is found to be 20−40 nm. Compared with the network α-Fe_2O_3−CNTs-1 architectures (Figure 1d), many more CNTs are attached in the α-Fe_2O_3 submicron spheres as for the network α-Fe_2O_3−CNTs-2 architectures (Figure 1g). We also observe that some attached CNTs

dx.doi.org/10.1021/am506238q | ACS Appl. Mater. Interfaces 2015, 7, 340−350

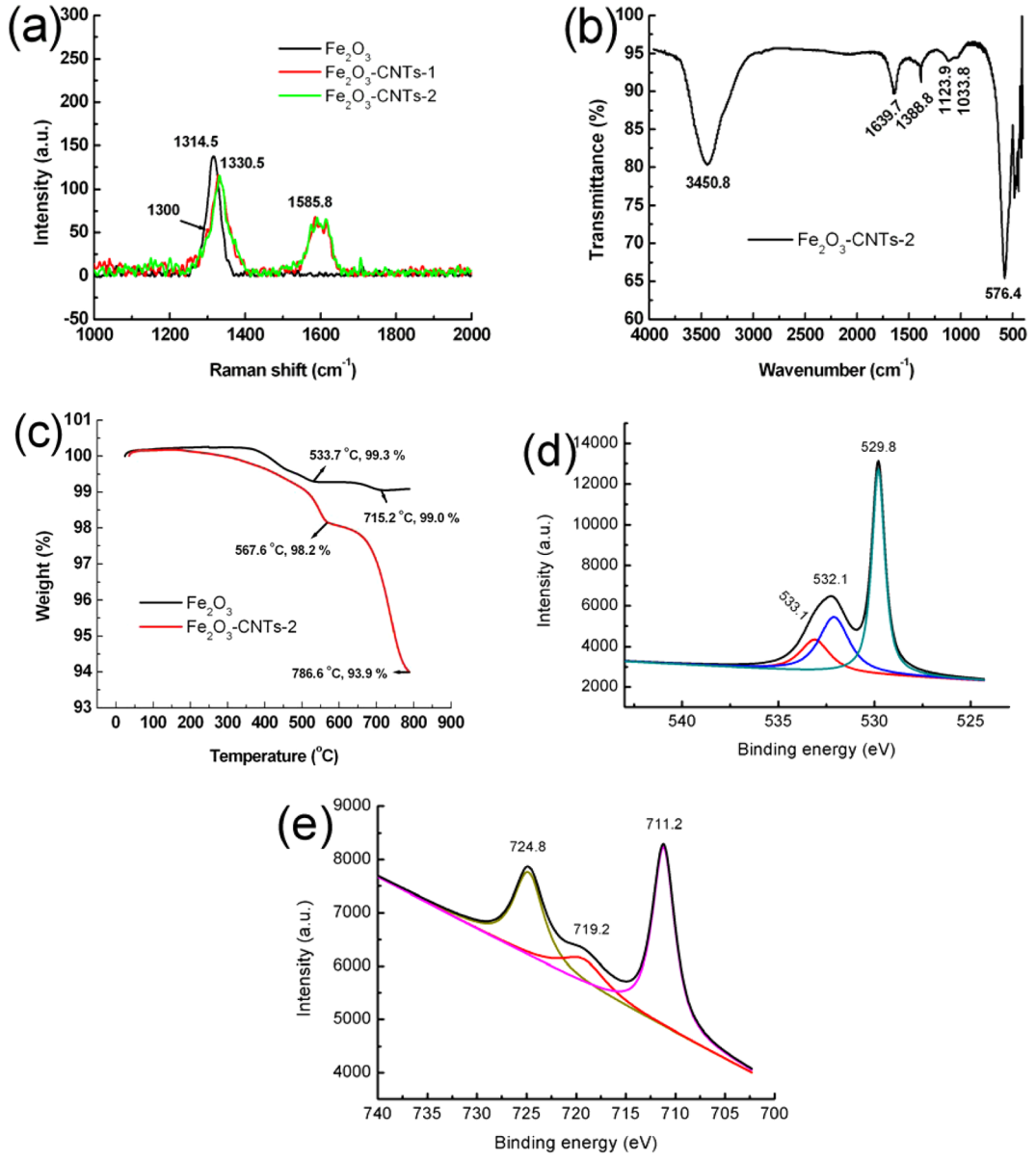

Figure 2. (a) Raman spectra, (b) FTIR spectra, (c) TGA curves in air, and XPS spectra of (d) O 1s region and (e) Fe 2p region for the α-Fe_2O_3–CNTs-2 samples.

exhibiting porous structure (Figure S5, Supporting Information), which arose from the oxidation of CNTs by mixed acid solution. The high-resolution transmission electron microscopy (HRTEM) image in Figure 1h shows the clear and continuous lattice fringe image for the α-Fe_2O_3 submicron spheres and CNTs, revealing the high crystallinity of network α-Fe_2O_3–CNTs architectures. As for the edge of α-Fe_2O_3, the distance of neighboring fringes was about 0.252 nm, which is close to that of (110) lattice spacing (0.251 nm) in the α-Fe_2O_3 structure. The selected area electron diffraction (SAED) pattern in Figure S6 (Supporting Information) shows the α-Fe_2O_3 has good single-crystalline structure, whereas the CNTs exhibit poly crystalline feature (Figure S7, Supporting Information). In solution, CATB can be dissociated into cations, $R(CH_3)_3–N^+$, and anions, Br^- ions. Numerous growing particles formed during the initial precipitated reaction. The surface of initial growing particles will be covered with CTAB, with its $R(CH_3)_3–N^+$ group absorbed on the surface of particles and its long hydrophobic alkyl chain outward, in order to reduce the attractive van der Waals or hard-sphere interactions. In our experiment, CTAB was expected to control the dispersion behavior of growing particles during the initial reaction process. F127 has a long chain polymer, and it was expected to control the orientation-assembly of the growing particles. Generally, F127 was used to synthesize the porous nanomaterials, but our experimental results confirmed that the presence of F127 did not lead to the formation of porous α-Fe_2O_3 nanomaterials. The exact reason is not clear, but we think the formation of porous nanomaterials is also related to the reaction conditions (e.g., temperature, time, and concentration), except for the addition of F127. If only CTAB or F127 (Figures S8 and S9, Supporting Information) was added in the hydrothermal reaction system (the synthetic procedure is similar to the synthesis of α-Fe_2O_3–CNTs-1), the synthesized α-Fe_2O_3–CNT hybrid composites are composed of numerous large-size α-Fe_2O_3 particles (over 500 nm). It is clearly seen that the

dx.doi.org/10.1021/am506238q | ACS Appl. Mater. Interfaces 2015, 7, 340–350

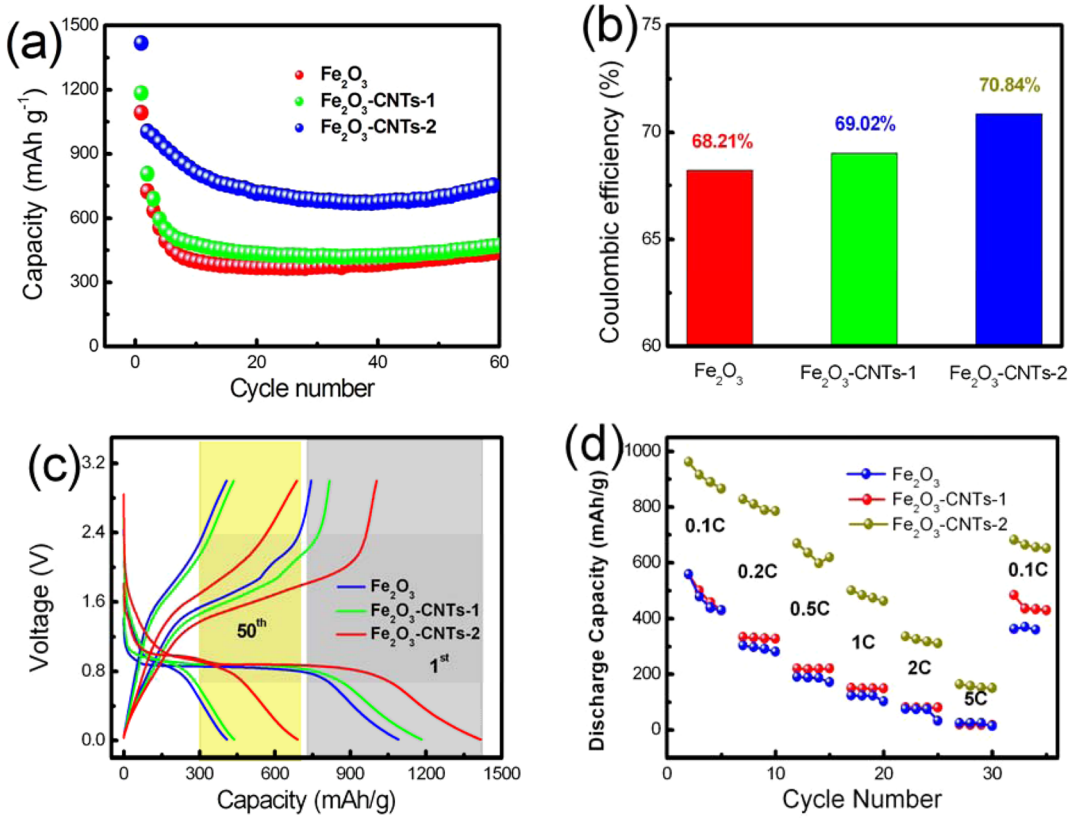

Figure 3. (a) Cycling performance, (b) the initial Coulombic efficiency, (c) discharge/charge profiles in the 1st and 50th cycles at a 0.2 C rate, and (d) the rate performance of the samples.

presence of only CTAB or F127 in the hydrothermal system will produce the formation of large-size α-Fe_2O_3 particles. As for the coexistence of CTAB and F127, the majority of α-Fe_2O_3 particles in the network α-Fe_2O_3−CNTs-1 were in the range of 250−350 nm. Moreover, we observed that the dispersion behavior of α-Fe_2O_3 particles in the network α-Fe_2O_3−CNTs-1 becomes poor. Evidently, the coexistence of CTAB and F127 in the hydrothermal system facilitates the formation of dispersed small-sized α-Fe_2O_3 particles, which will be helpful for the improvement of lithium storage performance.

Raman spectra of the synthesized α-Fe_2O_3 submicron spheres and network α-Fe_2O_3−CNT architectures are shown in Figure 2a. As for pure α-Fe_2O_3 submicron spheres, the characteristic peak of α-Fe_2O_3 was observed at 1314.5 cm^{-1}.[30] As for the network α-Fe_2O_3−CNT architectures, it is clearly seen that there are three peaks at 1300, 1330.5, and 1585.8 cm^{-1} which correspond to the characteristic peak of α-Fe_2O_3, the D band and G' band of CNTs, respectively. The Raman profiles for both network α-Fe_2O_3−CNTs-1 and network α-Fe_2O_3−CNTs-2 nearly overlapped, indicating that the increase of CNTs amount did not influence the chemical/physical properties of CNTs for the resulting composites. The D band is related to the defects and disorders in the hexagonal graphitic layers, whereas 'G'' band is related to vibration of sp^2-bonded carbon atoms in a two-dimensional hexagonal lattice.[31] The intensity ratio of the D and 'G'' band (I_D/I_G) of network α-Fe_2O_3−CNTs architectures is about 1.65, which is higher than that of the oxidized CNTs at 80 °C (1.13).[25] The increase of I_D/I_G ratio suggests that the surface defects of oxidized CNTs have an increasing trend after the hydrothermal reaction. On the other hand, the intensity of characteristic peak of α-Fe_2O_3 decreased significantly, indicating the crystallization degree of α-Fe_2O_3 components in the network α-Fe_2O_3−CNTs architectures become poor compared with the pure α-Fe_2O_3 submicron spheres. The main reason is attributed to the addition of the oxidized CNTs in the reaction system may influence the ordered self-assembly of the initial nuclei of α-Fe_2O_3 precipitates. Although the addition of CNTs in the reaction system lead to the crystallization decrease of α-Fe_2O_3 components in the network α-Fe_2O_3−CNTs architectures, they are favorable for improving the electrochemical performance of LIBs. The following coin cells tests also demonstrated that the capacity and rate performance of network α-Fe_2O_3−CNTs architectures have been significantly improved than the high crystallization α-Fe_2O_3 submicron spheres. Herein we also clarified that the increase of capacity and rate performance of nanocomposites are partially coming from the contribution of oxidized CNTs. In order to confirm the functional groups on the surface of network α-Fe_2O_3−CNTs-2 architectures, FTIR spectra were investigated in the wavenumber range of 400−4000 cm^{-1}, as shown in Figure 2b. The O−H stretching vibration peak can be observed at 3450.8 cm^{-1}, the C═O stretching vibration peak from carbonyl and carboxylic groups can be found at 1639.7 cm^{-1}, and the skeletal vibration peak of CNTs can be observed at 1388.8 cm^{-1}.[32] The peak at 1123.9 cm^{-1} can be assigned to the C−O−C stretching vibrations, and it my be arising from the surfactant of F127.[33] The peak at around 1033.8 cm^{-1} was attributed to the characteristic peaks of CTAB molecules.[34] The peak at 576.4 cm^{-1} may be attributed to the vibrations of Fe−O.[35] In the range of 400−700 cm^{-1}, it is clearly seen that there are three characteristic vibration peaks of α-Fe_2O_3, which are related to their structures

dx.doi.org/10.1021/am506238q | ACS Appl. Mater. Interfaces 2015, 7, 340−350

and sizes.[36] In order to evaluate the weight ratio between organic additives and inorganic α-Fe_2O_3 components, we analyzed the obtained samples using TGA measurements in the temperature range of 20−800 °C. Figure 2c shows the TGA curves in air for the synthesized α-Fe_2O_3 submicron spheres and network α-Fe_2O_3−CNTs-2 architectures. The TGA curves show that there are nearly no weight losses below 200 °C, indicating the samples were completely dried. As for α-Fe_2O_3 submicron spheres, the weight loss that takes place between 400 and 715.2 °C may possibly be ascribed to the removal of F127 and CTAB due to only the two kinds of surfactants were used in the hydrothermal reaction. Because the surface of α-Fe_2O_3 is not completely smooth (there are some pores or defects in α-Fe_2O_3), partial surfactant molecules may aggregate into the inner of pores or defects. In the range of 300−400 °C, the CTAB and F127 will be completely decomposed, but the produced gas cannot be rapidly removed from the interior of the pores or defects at a heating rate of 10 °C min^{-1}. Thus, the TGA curve presented a delaying behavior. As for the network α-Fe_2O_3−CNTs-2 architectures, the weight loss (1.8%) below 567.6 °C is higher than that of α-Fe_2O_3 submicron spheres. Except for the removal of CTAB molecules, the removal of labile oxygen functional groups on the surface of the oxidized CNTs may also contribute to this weight loss. At the temperature range of 567.6−786.6 °C, there is an obvious weight loss (4.3%) in the TGA curve, which can be attributed to the decomposition of CNTs. On the basis of the TGA curve, we calculate that the loading amount of CNTs in the α-Fe_2O_3−CNTs-2 composites is about 5.1%. As for the TGA curve of pure oxidized CNTs (Figure S10, Supporting Information), we can see that the oxidized CNTs can be completely decomposed after 800 °C. Figure 2d shows the O 1s X-ray photoelectron spectra (XPS) for the synthesized network α-Fe_2O_3−CNTs-2 architectures. There are three peaks in the curve: the sharp peak at 529.8 eV can be attributed to the oxygen in α-Fe_2O_3,[37] the peak at 532.1 eV can be assigned to the oxygen in the oxidized CNTs, and the peak at 533.1 eV can be ascribed to the oxygen in F127. Figure 2e shows the Fe 2p XPS spectrum for the synthesized network α-Fe_2O_3−CNTs-2 architectures. The main two peaks of Fe $2p_{3/2}$ and Fe $2p_{1/2}$ are at 711.2 and 724.8 eV, respectively, which is in good agreement with those of Fe_2O_3, and the satellite peak is at 719.2 eV, which is the characteristic peak of Fe^{3+} in Fe_2O_3.[38]

Figure 3a displays the long-time cycling performance of the synthesized α-Fe_2O_3 submicron spheres and network α-Fe_2O_3−CNT architectures at a rate of 0.2 C. As for α-Fe_2O_3 submicron spheres and network α-Fe_2O_3−CNTs-1, the specific capacity decreased significantly and was retained at 377.4 and 472.2 mAh g^{-1} after 11 cycles, respectively. After the following cycling, we note that the capacity has an increasing trend. The capacity of α-Fe_2O_3 submicron spheres and network α-Fe_2O_3−CNTs-1 reaches about 534.5 and 599.9 mAh g^{-1} at the 90th cycle, respectively. The increase of capacity can be assigned to the activation and stabilization of electrode materials, and the reversible growth polymer/gel-like film caused by the decomposition of the electrolyte at low potential.[39] In contrast, the network α-Fe_2O_3−CNTs-2 electrode shows the most remarkable performance. The specific capacity slowly decreased to 782.5 mAh g^{-1} after 11 cycles, and then presented an increasing trend. The capacity of network α-Fe_2O_3−CNTs-2 electrode arrived at 764.5 mAh g^{-1} at 60th cycle, which is almost 1.57 times than that of network α-Fe_2O_3−CNTs-2 electrode (486.6 mAh g^{-1}), and 1.78 times than that of α-Fe_2O_3 submicron spheres electrode (428.3 mAh g^{-1}). The initial Coulombic efficiency of network α-Fe_2O_3−CNTs-2 electrode (70.84%) is higher than that of network α-Fe_2O_3−CNTs-1 electrode (69.02%) and α-Fe_2O_3 submicron spheres electrode (68.21%), as shown in Figure 3b. Evidently, the electrochemical performance of network α-Fe_2O_3−CNTs-2 is significantly superior to α-Fe_2O_3 submicron spheres and network α-Fe_2O_3−CNTs-1. The reason could be that the addition of flexible and robust CNTs may improve the electronic conductivity of electrode and inhibit the large volume variation during charge/discharge process. On the other hand, the electrochemical performance of network α-Fe_2O_3−CNTs-1 is slightly higher than that of α-Fe_2O_3 submicron spheres, indicating that fewer CNTs do not facilitate the cross-linking of α-Fe_2O_3 particles. Figure 3c shows the discharge/charge profiles of the synthesized α-Fe_2O_3 submicron spheres and network α-Fe_2O_3−CNTs architectures at a rate of 0.2 C within the voltage window of 0.01−0.3 V. Their long voltage plateaus during the first discharge process were all located at ∼0.86 V and slightly increase at the 50th discharge process (0.95 V for network α-Fe_2O_3−CNTs-2, 0.92 V for network α-Fe_2O_3−CNTs-1, and 0.91 V for α-Fe_2O_3 submicron spheres), which is similar to previous reports.[40,41] It can be seen that the discharge capacities of α-Fe_2O_3 submicron spheres, network α-Fe_2O_3−CNTs-,1 and network α-Fe_2O_3−CNTs-2 in the 1st cycle are 1411.8, 1177.5, and 1088.3 mAh g^{-1}, respectively, and in the 50th cycle are 689.6, 438.5, and 404.9 mAh g^{-1}, respectively. The charge capacities of α-Fe_2O_3 submicron spheres, network α-Fe_2O_3−CNTs-1, and network α-Fe_2O_3−CNTs-2 in the 1st cycle are 1007.5, 820.7, and 745.3 mAh g^{-1}, respectively, and in the 50th cycle are 686.6, 435.8, and 402.3 mAh g^{-1}, respectively. The irreversible capacity loss can be mainly ascribed to the possible irreversible processes such as the decomposition of electrolyte, inevitable formation of the solid electrolyte interface (SEI) film and the formation of amorphous Li_2O.[42] It is interesting to note that the discharge capacities of electrodes in the first cycle all exceed the theoretical value of Fe_2O_3 (1005 mAh g^{-1}), which can be attributed to the decomposition of electrolyte, lithium storage on the surface of polymeric layer, or interfacial storage.[43] After the 50th cycle, the Coulombic efficiency of α-Fe_2O_3 submicron spheres, network α-Fe_2O_3−CNTs-1, and network α-Fe_2O_3−CNTs-2 increased to 99.6, 99.4, and 99.3%, respectively. The rate performance of α-Fe_2O_3 submicron spheres and network α-Fe_2O_3−CNTs was also investigated under different current densities, as shown in Figure 3d. It can be seen that the α-Fe_2O_3 submicron spheres exhibited lowest capacities of 485.3, 294.8, 185.4, 118.4, and 70.6 mAh g^{-1} at the current densities of 0.1, 0.2, 0.5, 1, and 2 C, respectively. The network α-Fe_2O_3−CNTs-1 showed higher capacities of 496.4, 333.8, 222.1, 154.8, and 87.4 mAh g^{-1} at the current densities of 0.1, 0.2, 0.5, 1, and 2 C, respectively. It is clear that the rate performance of network α-Fe_2O_3−CNTs-1 is better than that of α-Fe_2O_3 submicron spheres. In a high current density of 5 C, both α-Fe_2O_3 submicron spheres and network α-Fe_2O_3−CNTs-1 experience significant capacity fading, and only ∼20.1 mAh g^{-1} can be obtained. This may be attributed to the low conductivity and the aggregation of iron oxides particles during the cycling process. The electrodes prepared with α-Fe_2O_3 submicron spheres and network α-Fe_2O_3−CNTs-1 were easily loosened and sloughed off,[44] leading to the loss of active materials and making the cells invalid. However, network α-Fe_2O_3−CNTs-2 composite displayed a much better stability and electrochemical perform-

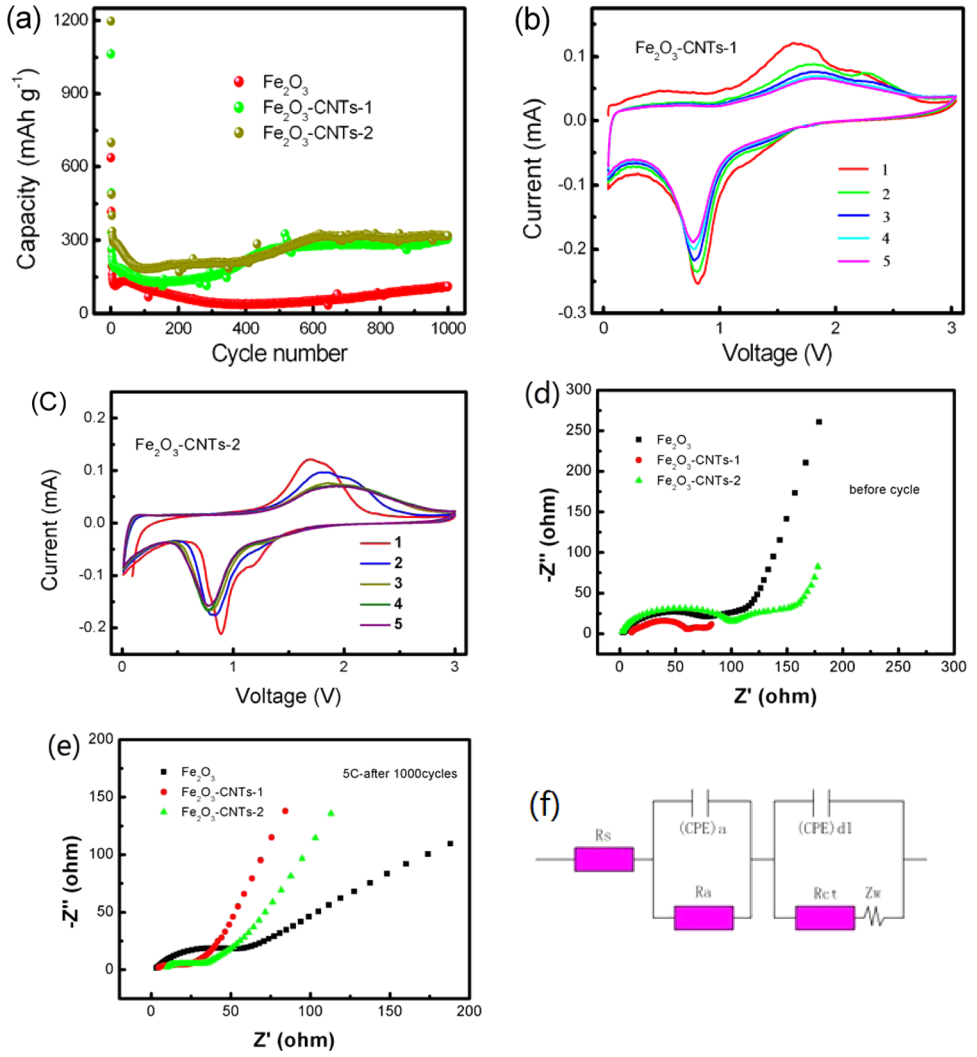

Figure 4. (a) Long-term cycling performance of samples at a high current density of 5 C, cyclic voltammogram profiles of network (b) α-Fe_2O_3−CNTs-1 composite, and (c) α-Fe_2O_3−CNTs-2 composite, EIS spectra of samples (d) before cycling and (e) after 1000 cycles at the current density of 5 C, and (f) an electrochemical equivalent circuit.

ance. It presented high capacities of 907.9, 798.9, 625.3, 479.5, and 322.7 mAh g^{-1} at the current densities of 0.1, 0.2, 0.5, 1, and 2 C, respectively. Even at a high current density of 5 C, the capacity still exhibited as high as 168.5 mAh g^{-1}, which is more than 8 times than that of α-Fe_2O_3 submicron spheres and network α-Fe_2O_3−CNTs-1. This suggests that the introduction of a suitable amount CNTs may significantly enhance the rate performance. When returning to the initial current density of 0.1 C, the network α-Fe_2O_3−CNTs-2 composite returns to a high capacity of 667.3 mAh g^{-1}. The reasons for the high capacity of the network α-Fe_2O_3−CNTs-2 composite are that (1) the introduction of oxidized CNTs can enhance the electronic conductivity of network α-Fe_2O_3−CNTs-2 composite, improve the charge transfer between the electrode and electrolyte, and trap extra Li^+ via the inner holes and defects of the oxidized CNTs in the discharge process; the defects on the surface of CNTs arise from the oxidation of CNTs in the mixed acid solution; (2) the addition of CNTs could acted as an excellent cushion to tolerate the large volume variation and inhibit the severe particles aggregation during the repeated charge/discharge cycling process; and (3) network CNTs act as the flexible and robust backbone for α-Fe_2O_3−CNTs-2 composite. Furthermore, the CNTs are in situ attached to the α-Fe_2O_3 particles. Such special structure of network α-Fe_2O_3−CNTs-2 composite is beneficial for maintaining the structural integrity of electrode and improving the cycling performance.

To evaluate the long-term cycling performance of samples, we cycled cells at high current density of 5 C over 1000 cycles, as shown in Figure 4a. As for the α-Fe_2O_3 submicron spheres, the capacity quickly decreased in the eighth cycles (137.8 mAh g^{-1}). Then the decreasing trend become slowly after the following cycling, and the capacity fade to ∼37.3 mAh g^{-1} at the 400th cycle. After that, the capacity exhibited an increasing trend and gradually reached at ∼116.7 mAh g^{-1} at the 1000th cycle. As for network α-Fe_2O_3−CNTs-1 composite, the capacity fading trend is similar to α-Fe_2O_3 submicron spheres before the 118th cycle (134.9 mAh g^{-1}). At the following cycling, the capacity gradually increased to ∼271 mAh g^{-1} at the 477th cycle and arrived at ∼311.2 mAh g^{-1} at the 1000th cycle. As for the network α-Fe_2O_3−CNTs-2 composite, the capacity was significantly higher than that of α-Fe_2O_3 submicron spheres and α-Fe_2O_3−CNTs-1 composite, and the capacity maintained at ∼220.2 mAh g^{-1} before the 400th cycle. With the further increase of cycling, the capacity arrived at ∼326.5 mAh g^{-1} at the 615th cycle and retained this value until

dx.doi.org/10.1021/am506238q | ACS Appl. Mater. Interfaces 2015, 7, 340−350

Table 1. Electrochemical Parameters Obtained from EIS Tests before and after Cycling

	specimen	R_s ($\Omega\cdot cm^2$)	Y_a ($\Omega^{-1}cm^{-2}s^n10^{-4}$)	n_a	R_a ($\Omega\cdot cm^2$)	Y_{dl} ($\Omega^{-1}cm^{-2}s^n10^{-4}$)	n_{dl}	R_{ct} ($\Omega\cdot cm^2$)
before cycling	α-Fe_2O_3	2.32	1.14	0.65	97.68	55.11	0.76	0.01
	α-Fe_2O_3–CNTs-2	0.85	22.57	0.79	29.84	0.14	0.75	95.31
after 1000 cycles	α-Fe_2O_3–CNTs-2	0.24	12.58	0.32	40.41	91.59	0.65	0.01

1000th cycle. The cycling tests showed that the electrochemical performance of network α-Fe_2O_3–CNTs-2 composite is significantly superior to α-Fe_2O_3 submicron spheres and network α-Fe_2O_3–CNTs-1 composite at relatively short-term cycling (400 cycles), and slightly superior to the network α-Fe_2O_3–CNTs-1 composite at long-term cycling (1000 cycles). This phenomenon confirms that (1) the introduction of CNTs may significantly improve the electrochemical performance of iron oxides particles at high current density, and (2) larger amount CNTs are significantly beneficial for the increase of capacity in the relatively short-term cycling (400 cycles), but the variation of CNTs amounts for the increase of capacity is not evident in the long term cycling (1000 cycles). Figure 4b shows the cyclic voltammogram (CV) curves of network α-Fe_2O_3–CNTs-1 composite under a scan rate of 0.1 mVs^{-1} at room temperature. It can be found that there are two reduction peaks (0.82 and 1.22 V) in the first cathodic sweep process—a bulky peak and a tiny broad peak. This can be attributed to the two lithiation processes,[45] which are related to the reduction reaction of Fe^{3+} or Fe^{2+} to Fe^0 and the irreversible reaction with the electrolyte.[46] In the first step, a lithium will be inserted into the α-Fe_2O_3 components in the network α-Fe_2O_3–CNTs-1 composite to form cubic $Li_2Fe_2O_3$ (α-$Fe_2O_3 + 2Li^+ + 2e^- \rightarrow Li_2Fe_2O_3$). Second, Fe^{2+} will be reduced to Fe^0 and accompanying the decomposition of electrolyte ($Li_2Fe_2O_3 + 4Li^+ + 4e^- \rightarrow 2Fe + 3Li_2O$), and formation of amorphous Li_2O particles which are deemed as the main reason for the irreversible capacity during the discharge process.[47] In the anodic process, two oxidation peaks located at 1.64 and 2.19 V are observed which are related to the oxidation of Fe^0 to Fe^{2+} and Fe^{3+} to reform Fe_2O_3.[48] In the second cycle, the peak located at 1.22 V disappeared and only one peak at 0.79 V was observed in the cathodic sweep. This can be ascribed to the irreversible phase transformation from α-$Li_xFe_2O_3$ to cubic $Li_2Fe_2O_3$ and the formation of SEI film.[49] In addition, we found that the oxidation peaks shift from 1.64 and 2.19 V to 1.79 and 2.29 V, respectively. During the following cycles, the position and integrated area of reduction and oxidation peaks remain nearly unchanged, indicating the good reversibility reaction between Fe^0 and Fe^{2+}. Figure 4c shows the CV curves of network α-Fe_2O_3–CNTs-2 composite under a scan rate of 0.1 mVs^{-1} at room temperature. There are two reduction peaks (0.79 and 1.19 V) in the first cathodic sweep process—a bulky peak and a broad peak. The intensity of broad peak located at 1.19 V becomes stronger than that of α-Fe_2O_3–CNTs-1 composite. In the second cycle, the peak located at 1.19 V disappeared and the peak at 0.79 V still exits. In the anodic process, two peaks (1.69, 1.86 V) are observed. This can be attributed to the oxidation of Fe^0 to Fe^{2+} and Fe^{3+} to reform Fe_2O_3. The oxidation peaks shift from 1.69 and 1.86 V to 1.79 and 2.11 V, respectively. In the third cycle, the intensity of two oxidation peaks decreased but the peak location does not change significantly. At the following cycles, the position and integrated area of reduction and oxidation peaks nearly overlapped, suggesting the good reversibility reaction between Fe^0 and Fe^{2+}. To evaluate the electrochemical dynamical behaviors of samples before and after cycling, we carried out electrochemical impedance spectroscopy (EIS) measurements, as shown in Figure 4d,e. The EIS spectra of α-Fe_2O_3 submicron spheres and network α-Fe_2O_3–CNTs composites are composed of a depressed quasi-semicircle in the range of high to middle frequency and a straight sloping line in the low frequency range. The capacitive arc diameter was acting as the resistance, and the sloped line was related to the Warburg impedance (Z_w) of lithium ion diffusion. The EIS plots are approximately semicircle shaped in the complex plane with the center under the real axis. The depressed quasi-semicircle was similar to a capacitor, which indicates (a) a homogeneous SEI film was formed on the electrode surface and (b) a typical behavior for solid electrodes that presented the frequency dispersion of impedance data. After 1000 cycles, the capacitive arc diameter of network α-Fe_2O_3–CNTs-2 composite is significantly reduced than that of α-Fe_2O_3 submicron spheres, indicating the electrochemical dynamic behavior and cycling capability of network α-Fe_2O_3–CNTs-2 composite are much better than that of α-Fe_2O_3 submicron spheres. Figure 4f shows the electrochemical equivalent circuit model according to the simulation. R_s is the solution resistance, R_a is SEI film resistance, and R_{ct} is charge transfer resistance. C_a and C_{dl} are SEI film capacitance and double-layer capacitance, respectively. To compensate the nonhomogeneity of electrode surface,[50] we substituted a constant phase element (CPE) for C_a and C_{dl}, respectively, in the electrochemical equivalent circuit process. Y and n are the parameters of CPE, and the unit of Y is $\Omega^{-1}cm^{-2}s^n$ and n reflecting a phase shift satisfying the condition $0 \leq n \leq 1$, $s = i\omega$ where i is $\sqrt{-1}$ and ω is the angular frequency.[51,52] Y can be regarded to be approximation to the value of capacitance. The parameters associated with EIS are listed in Table 1. As for α-Fe_2O_3 submicron spheres and network α-Fe_2O_3–CNTs-2 composite, R_a is 97.68 and 29.84 $\Omega\cdot cm^2$, respectively. The low R_a of α-Fe_2O_3–CNTs-2 composite is beneficial to enhance the Li^+ transmission in the SEI film and provide efficient electrical conductive networks. Owing to the surface of oxidized CNTs has much oxygen-containing functional groups, the α-Fe_2O_3–CNTs-2 composite can compactly bond to the electrode surface than that of the α-Fe_2O_3 submicron spheres. It will be helpful for the improvement of the adhesion force between the active materials and electrode surface. Figure S11 (Supporting Information) shows the optical image of the α-Fe_2O_3 submicron spheres, α-Fe_2O_3–CNTs-1 and α-Fe_2O_3–CNTs-2 composites after cycling at 0.2 C. It is clear that the active materials for α-Fe_2O_3 submicron spheres were easily abrupt from the copper foil. On the other hand, the improvement of adhesion force between the active materials and electrode surface will influence the double layer capacitance and lead to the increase of charge transfer resistance (R_{ct}). As for α-Fe_2O_3 submicron spheres and α-Fe_2O_3–CNTs-2 composites, the R_{ct} value before cycling is 0.01 and 95.31 $\Omega\cdot cm^2$, respectively. This suggests that the addition of oxidized CNTs in composites has improved the adhesion force between the active materials and electrode surface. This was possibly the main reason that the introduction of oxidized

CNTs in the composites led to the increase of resistance over that of α-Fe_2O_3 submicron spheres electrode in the middle and high frequencies, and the capacitance behavior in the low frequency does not present the improvement than α-Fe_2O_3 submicron spheres electrode. After 1000 cycles, the R_a value of network α-Fe_2O_3−CNTs-2 composite has a slight increase (40.41 $\Omega \cdot cm^2$), suggesting the quality of SEI film has been improved. This can be attributed to the variation of morphology and microstructure of SEI film during the repeated cycling. The Y_a value of network α-Fe_2O_3−CNTs-2 composite decreased from 22.57 to 12.58 Ω^{-1} cm^{-2} s^n 10^{-4} after 1000 cycles, indicating the thickness of SEI film has an increasing trend. The variation of the n_a value resulted in the modification of the chemical composition film. The n_a value of network α-Fe_2O_3−CNTs-2 composite before cycling was ∼0.79, suggesting the SEI film was relatively homogeneous. After 1000 cycles, the n_a value decreased to ∼0.32, indicating that the SEI film becomes loose and porous, as suggested by the values of R_{ct} before cycling (95.31 $\Omega \cdot cm^2$) and after cycling (0.01 $\Omega \cdot cm^2$). This evolution can be explained by an increase of cycling leading to the appearance of defects and/or pores in the SEI film, which facilitates the Li^+ into and from the film. Evidently, the network α-Fe_2O_3−CNTs-2 composite can significantly enhance the cycling stability and rate performance perhaps benefited from its unique network structural characteristics. The electronic conductivity measurements of the samples was done at room temperature using the four-probe method (Keithley 2636A). As for the CNTs, the electronic conductivity of CNTs is 13.8 S/cm. After the chemical modification of CNTs by mixed acid, the electronic conductivity of oxidized CNTs is 2.5 S/cm. As for the synthesized α-Fe_2O_3−CNTs, the electronic conductivity is 1.7 S/cm. It was known that the Fe_2O_3 has a poor electronic conductivity (e.g., γ-Fe_2O_3 < 10^{-6} S/cm). The addition of oxidized CNTs will significantly improve the electronic conductivity of Fe_2O_3-based hybrid materials.

Different from previous publications,[53] herein, we used the agglomerated CNTs as raw materials. It is known that the agglomerated CNTs are in a severely agglomeration state, the numerous 1-D nanotubes are tangled each other and formation of large-sized agglomerates. We applied the mixed acid oxidation and hydrothermal treatment strategy to disperse the agglomerated CNTs into a well-ordered state. Our results indicated that the agglomerated CNTs can be well attached to the α-Fe_2O_3 particles and form network α-Fe_2O_3−CNTs architectures. Our electrochemical results showed that the synthesized network α-Fe_2O_3−CNTs architectures exhibit good performance, but the microstructure and compositions (e.g., reducing the Fe_2O_3 particle sizes and controlling the amount of CNTs in composites and the oxidization time for the agglomerated CNTs) still need further optimizing in order to get a better performance. Generally, the SEI film is formed at a voltage less than 1 V (vs Li^+/Li) because there is no electrolyte system stable at that range. During the first cycle, the peak around 0.8 V represents such reaction. When the SEI film is formed, this reaction is typically suppressed, indicating that a stable process formed. Figure 5a shows the TEM image of α-Fe_2O_3 submicron spheres after 50 cycles at a rate of 0.2 C. It can be seen that the general morphology of samples does not change significantly after cycling, but we can see that a thin layer film is formed on the surface of α-Fe_2O_3 submicron spheres after cycling. The thickness of thin layer film the ∼5 nm, as shown in Figure 5b. From higher TEM image, the thin

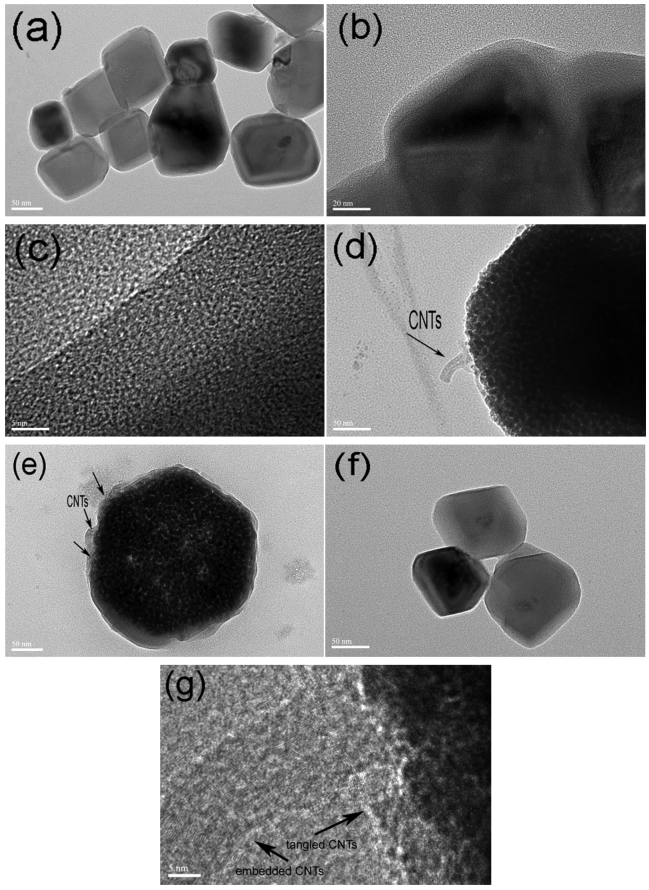

Figure 5. (a−c) TEM images of the α-Fe_2O_3 submicron spheres after 50 cycles at a rate of 0.2 C, (d−g) TEM and HRTEM images of the hybrid α-Fe_2O_3−CNTs-1 composites after 50 cycles at a rate of 0.2 C.

layer film (Figure 5c) exhibited amorphous characteristics, whereas the α-Fe_2O_3 substrate presented single-crystalline structure (Figure S12, Supporting Information). We also observe the morphology evolution of hybrid network α-Fe_2O_3−CNTs-1 composites after 50 cycles at a rate of 0.2 C. Interestingly, we observed that those α-Fe_2O_3 particles that were successfully attached to CNTs are completely disassembled into the assemblies composed of numerous small-sized particles (5−10 nm; Figure 5d,e and Figure S13, Supporting Information), whereas those α-Fe_2O_3 particles that were not successfully attached to CNTs will maintain their structures well (Figure 5f). Figure 5g clearly shows the CNTs are attached in the α-Fe_2O_3 submicron spheres, and the α-Fe_2O_3 particles are also tangled by CNTs. The TEM images indicated that the inserting of CNTs into α-Fe_2O_3 particles will induce the disassembly of bigger submicron particles from an integrated one into the assemblies composed of numerous nanoparticles (5−10 nm), which was regarded as one of the main reason to enhance the lithium storage capacity. Yu et al. reported the electrochemical property of Fe_2O_3 nanoparticles-filled carbon nanotubes.[46] The electrochemical tests showed that the Fe_2O_3-filled CNTs exhibted a reversible charge capacity of 648.6 mAh g^{-1} at a rate of 60 mA g^{-1}. At a high rate of 1200 mA g^{-1}, a capacity of 335 mAh g^{-1} can be achieved. When the current rate is returned to 60 mA g^{-1}, a capacity of 603 mAh g^{-1} can be achieved. Xiao et al. reported the single-crystalline mesoporous α-Fe_2O_3 and Fe_3O_4 nanorods as anode materials for LIBs. The rate performance tests showed

that the discharge capacity is reduced to 980, 915, 820 mAh g^{-1} at rates of 0.1, 0.2 and 0.5 C, respectively.[49] According to the electrochemical data, it is clearly seen that our synthesized hybrid network α-Fe_2O_3−CNTs composites are not the best materials for Fe_2O_3 based electrodes. However, it is still comparable with the state-of-the-art of Fe_2O_3 based electrodes with good cycling and rate performance. The capacity of hybrid network α-Fe_2O_3−CNTs composites can maintain at ∼220.2 mAh g^{-1} before the 400th cycle, arrived at ∼326.5 mAh g^{-1} in the 615th cycle and retained this value until 1000th cycle. To validate that the addition of CNTs in the α-Fe_2O_3−CNTs hybrid composites could tolerate the large volume variation and inhibit the severe particles aggregation, we investigated the cross-sectional images of α-Fe_2O_3 particles and α-Fe_2O_3−CNTs hybrid composites after cycling 50 cycles at a rate of 0.2 C. It is clearly seen that the pure α-Fe_2O_3 particles electrodes after cycling (Figure S14, Supporting Information) are loose and easily break off from the substrates. As for α-Fe_2O_3−CNTs hybrid composites, the α-Fe_2O_3−CNTs hybrid composites after cycling could form network architectures and the α-Fe_2O_3 particles are encapsulated in the substrates (Supporting Information, Figure S15 for α-Fe_2O_3−CNTs-1 and Figure S16 for α-Fe_2O_3−CNTs-2). The cross-sectional images of α-Fe_2O_3 particles and α-Fe_2O_3−CNTs hybrid composites after cycling indicated that the α-Fe_2O_3−CNTs hybrid composites could tolerate the large volume variation and inhibit the severe particles aggregation, which will be a benefit for the improvement of electrochemical performance. Compared with pure α-Fe_2O_3 submicron spheres, our synthesized hybrid network α-Fe_2O_3−CNTs composites exhibited excellent electrochemical performance.

4. CONCLUSIONS

In summary, we have successfully developed a facile hydrothermal method for the synthesis of network α-Fe_2O_3−CNTs hybrid architectures. As for the pure α-Fe_2O_3 submicron spheres, the capacity decreased significantly and retained at 377.4 mAh g^{-1} at 11 cycles. In contrast, the capacity of network α-Fe_2O_3−CNTs-2 (764.5 mAh g^{-1}) is 1.78 times than that of α-Fe_2O_3 submicron spheres (428.3 mAh g^{-1}) at the 60th cycle. After long-term 1000 cycles at a high current density of 5 C, the capacity of α-Fe_2O_3 submicron spheres fade to ∼37.3 mAh g^{-1} at the 400th cycle and gradually increased to ∼116.7 mAh g^{-1} at the 1000th cycle, whereas the capacity of network α-Fe_2O_3−CNTs-2 maintained at ∼220.2 mAh g^{-1} before the 400th cycle arrived at ∼326.5 mAh g^{-1} at the 615th cycle and retained this value until 1000th cycle. Our results confirm that the synthesized network α-Fe_2O_3−CNTs composites could significantly enhance the cycling and rate performance over that of pure α-Fe_2O_3 composite. The three-dimensional network architectures are promising candidates for anode materials for LIBs in the near future.

■ ASSOCIATED CONTENT

Supporting Information

XRD patterns, VSM analysis, and TEM, HRTEM, and SAED images. This material is available free of charge via the Internet at http://pubs.acs.org.

■ AUTHOR INFORMATION

Corresponding Authors

*E-mail: guogao@sjtu.edu.cn.
*E-mail: dxcui@sjtu.edu.cn.

Author Contributions

The manuscript was written through contributions of all authors. All authors have given approval to the final version of the manuscript.

Notes

The authors declare no competing financial interest.

■ ACKNOWLEDGMENTS

We thank the Chinese 973 Project (2010CB933901), the National Natural Science Foundation of China (Nos. 81225010, 21306102, 81327002, and 81101169), and 863 High-Tech project of China (2014AA020701) for financial support. The authors are also grateful for the Instrumental Analytical Center of Shanghai Jiao Tong University.

■ REFERENCES

(1) Dhillon, R. S.; George von, W. Mitigation of Global Warming through Renewable Biomass. *Biomass Bioenergy* **2013**, *48*, 75−89.
(2) Willem, P. N.; Christopher, J. C. Implications of Fossil Fuel Constraints on Economic Growth and Global Warming. *Energy Policy* **2009**, *37*, 166−180.
(3) Zhang L.; Wu H. B.; Lou X. W. Iron-Oxide-based Advanced Anode Materials for Lithium-Ion Batteries *Adv. Energy Mater.* **2014**, *4*, DOI: 10.1002/aenm.201300958.
(4) Gao, G.; Yu, L.; Wu, H. B.; Lou, X. W. Hierarchical Tubular Structures Constructed by Carbon-Coated α-Fe_2O_3 Nanorods for Highly Reversible Lithium Storage. *Small* **2014**, *10*, 1741−1745.
(5) Wang, B.; Wu, H. B.; Zhang, L.; Lou, X. W. Self-Supported Construction of Uniform Fe_3O_4 Hollow Microspheres from Nanoplate Building Blocks. *Angew. Chem., Int. Ed.* **2013**, *52*, 4165−4168.
(6) Zhang, L.; Wu, H. B.; Madhavi, S.; Hng, H. H.; Lou, X. W. Formation of Fe_2O_3 Microboxes with Hierarchical Shell Structures from Metal-Organic Frameworks and Their Lithium Storage Properties. *J. Am. Chem. Soc.* **2012**, *134*, 17388−17391.
(7) Ji, L.; Lin, Z.; Alcoutlabi, M.; Zhang, X. Recent Developments in Nanostructrured Anode Materials for Rechargeable Lithium-ion Batteries. *Energy Environ. Sci.* **2011**, *4*, 2682−2699.
(8) Amatucci, G. G.; Tarascon, J. M.; Klein, L. C. The End Member of the Li_xCoO_2 Solid Solution. *J. Electrochem. Soc.* **1996**, *143*, 1114−1123.
(9) Palacin, M. R. Recent Advances in Rechargeable Battery Materials: A Chemist's Perspective. *Chem. Soc. Rev.* **2009**, *38*, 2565−2575.
(10) Scrosati, B.; Hassoun, J.; Sun, Y. K. Lithium-Ion Batteries. A Look into the Future. *Energy Environ. Sci.* **2011**, *4*, 3287−3295.
(11) Bogart, T. D.; Oka, D.; Lu, X.; Gu, M.; Wang, C.; Korgel, B. A. Lithium Ion Battery Performance of Silicon Nanowires with Carbon Skin. *ACS Nano* **2014**, *8*, 915−922.
(12) Zhang, Q.; Uchaker, E.; Candelaria, S. L.; Cao, G. Nanomaterials for Energy Conversion and Storage. *Chem. Soc. Rev.* **2013**, *42*, 3127−3171.
(13) Duan, B.; Wang, W.; Wang, A.; Yu, Z.; Zhao, H.; Yang, Y. A New Lithium Secondary Battery System: The Sulfur/Lithium-ion Battery. *J. Mater. Chem. A* **2014**, *2*, 308−314.
(14) Gao, M. R.; Xu, Y. F.; Jiang, J.; Yu, S. H. Nanostructured Metal Chalcogenides: Synthesis, Modification, and Applications in Energy Conversion and Storage Devices. *Chem. Soc. Rev.* **2013**, *42*, 2986−3017.
(15) Lotfabad, E. M.; Ding, J.; Cui, K.; Kohandehghan, A.; Kalisvaart, W. P.; Hazelton, M.; Mitlin, D. High-Density Sodium and Lithium Ion Battery Anodes from Banana Peels. *ACS Nano* **2014**, *8*, 7115−7129.
(16) Zhou, G.; Pei, S.; Li, L.; Wang, D. W.; Wang, S.; Huang, K.; Yin, L. C.; Li, F.; Cheng, H. M. A Graphene−Pure-Sulfur Sandwich Structure for Ultrafast, Long-Life Lithium−Sulfur Batteries. *Adv. Mater.* **2014**, *26*, 625−631.

(17) Park, Y.; Shin, D. S.; Woo, S. H.; Choi, N. S.; Shin, K. H.; Ho, S. M.; Lee, K. T.; Hong, S. Y. Sodium Terephthalate as Organic Anode Material for Sodium Ion Batteries. *Adv. Mater.* **2012**, *24*, 3562−3567.
(18) Fu, K.; Yildiz, O.; Bhanushali, H.; Wang, Y.; Stano, K.; Xue, L.; Zhang, X.; Bradford, P. D. Aligned Carbon Nanotube−Silicon Sheets: A Novel Nano-architecture for Flexible Lithium Ion Battery Electrodes. *Adv. Mater.* **2013**, *25*, 5109−5114.
(19) Wang, B.; Li, X.; Zhang, X.; Luo, B.; Zhang, Y.; Zhi, L. Contact-Engineering Void-Involved Silicon/Carbon Nanohybrids as Lithium-Ion Battery Anodes. *Adv. Mater.* **2013**, *25*, 3560−3565.
(20) Zhou, G.; Wang, D. W.; Hou, P. X.; Li, W.; Li, N.; Liu, C.; Li, F.; Cheng, H. M. A Nanosized Fe_2O_3 Decorated Single-Walled Carbon Nanotube Membrane as a High-performance Flexible Anode for Lithium Ion Batteries. *J. Mater. Chem.* **2012**, *22*, 17942−17946.
(21) Chen, J.; Xu, L. N.; Li, W. Y.; Gou, X. L. α-Fe_2O_3 Nanotubes in Gas Sensor and Lithium-ion Battery Applications. *Adv. Mater.* **2005**, *17*, 582−586.
(22) Qu, Q.; Yang, S.; Feng, X. 2D Sandwich-like Sheets of Iron Oxide Grown on Graphene as High Energy Anode Materials for Supercapacitors. *Adv. Mater.* **2011**, *23*, 5574−5580.
(23) Qin, L.; Zhu, Q.; Li, G.; Liu, F.; Pan, Q. Controlled Fabrication of Flower-like ZnO-Fe_2O_3 Nanostructures Films with Excellent Lithium Storage Properties Through a Partly Sacrificed Template Method. *J. Mater. Chem.* **2012**, *22*, 7544−7550.
(24) Gao, G.; Zhang, Q.; Wang, K.; Song, H.; Qiu, P.; Cui, D. Axial Compressive α-Fe_2O_3 Microdisks Prepared from CSS Template for Potential Anode Materials of Lithium Ion Batteries. *Nano Energy* **2013**, *2*, 1010−1018.
(25) Zhao, M. Q.; Peng, H. J.; Tian, G. L.; Zhang, Q.; Huang, J. Q.; Cheng, X. B.; Tang, C.; Wei, F. Hierarchical Vine-Tree-like Carbon Nanotube Architectures: In Situ CVD Self-Assembly and Their Use as Robust Scaffolds for Lithium−Sulfur Batteries. *Adv. Mater.* **2014**, *26* (41), 7051−7058.
(26) Gao, G.; Qiu, P.; Qian, Q.; Zhou, N.; Wang, K.; Song, H.; Fu, H.; Cui, D. PEG-200-Assisted Hydrothermal Method for the Controlled-Synthesis of Highly Dispersed Fe_3O_4 Nanoparticles. *J. Alloys Compd.* **2013**, *574*, 340−344.
(27) Jia, X.; Chen, Z.; Suwarnasarn, A.; Rice, L.; Wang, X.; Sohn, H.; Zhang, Q.; Wu, B. M.; Wei, F.; Lu, Y. High-Performance Flexible Lithium-Ion Electrodes Based on Robust Network Architectures. *Energy Environ. Sci.* **2012**, *5*, 6845−6849.
(28) Li, X.; Qiao, L.; Li, D.; Wang, X.; Xie, W.; He, D. Three-Dimensional Network Structured α-Fe_2O_3 Made from a Stainless Steel Plate As a High-Performance Electrode for Lithium Ion Batteries. *J. Mater. Chem. A* **2013**, *1*, 6400−6406.
(29) Wei, F.; Zhang, Q.; Qian, W. Z.; Yu, H.; Wang, Y.; Luo, G. H.; Xu, G. H.; Wang, D. Z. The Mass Production of Carbon Nanotubes Using a Nano-agglomerate Fluidized Bed Reactor: A Multiscale Space−Time Analysis. *Powder Technol.* **2008**, *183*, 10−20.
(30) Zhang, X.; Niu, Y.; Meng, X.; Li, Y.; Zhao, J. Structural Evolution and Characteristics of the Phase Transformations Between α-Fe_2O_3, Fe_3O_4 and γ-Fe_2O_3 Nanoparticles under Reducing and Oxidizing Atmospheres. *CrystEngComm* **2013**, *15*, 8166−8172.
(31) Tuinstra, F.; Koenig, J. L. Raman Spectrum of Graphite. *J. Chem. Phys.* **1970**, *53*, 1126.
(32) Si, Y. C.; Samulski, E. T. Synthesis of Water Soluble Graphene. *Nano Lett.* **2008**, *8*, 1679−1682.
(33) Xu, Y. Z.; Bai, H.; Lu, G. W.; Li, C.; Shi, G. Q. Flexible Graphene Films via the Filtration of Water-Soluble Noncovalent Functionalized Graphene Sheets. *J. Am. Chem. Soc.* **2008**, *130*, 5856−5857.
(34) Wang, S.; Xu, H.; Qian, L.; Jia, X.; Wang, J.; Liu, Y.; Tang, W. CTAB-assisted Synthesis and Photocatalytic Property of CuO Hollow Microspheres. *J. Solid State Chem.* **2009**, *182*, 1088−1093.
(35) Alibeigi, S.; Vaezi, M. R. Phase Transformation of Iron Oxide Nanoparticles by Varying the Molar Ratio of Fe^{2+}:Fe^{3+}. *Chem. Eng. Technol.* **2008**, *31*, 1591−1596.
(36) Han, Q.; Liu, Z.; Xu, Y.; Chen, Z.; Wang, T.; Zhang, H. Growth and Properties of Single-Crystalline γ-Fe_2O_3 Nanowires. *J. Phys. Chem. C* **2007**, *111*, 5034−5038.
(37) Wu, P.; Xu, Z. Silanation of Nanostructured Mesoporous Magnetic Particles for Heavy Metal Recovery. *Ind. Eng. Chem. Res.* **2005**, *44*, 816−824.
(38) Fujii, T.; de Groot, F. M. F.; Sawatzky, G. A.; Voogt, F. C.; Hibma, T.; Okada, K. In Situ XPS Analysis of Various Iron Oxide Films Grown by NO_2-Assisted Molecular Beam Epitaxy. *Phys. Rev. B* **1999**, *59*, 3195−3202.
(39) Lee, J. E.; Yu, S.-H.; Lee, D. J.; Lee, D.-C.; Han, S. I.; Sung, Y.-E.; Hyeon, T. Facile and Economical Synthesis of Hierarchical Carbon-Coated Magnetite Nanocomposite Particles and Their Applications in Lithium Lon Battery Anodes. *Energy Environ. Sci.* **2012**, *5*, 9528−9533.
(40) Chen, S.; Bao, P.; Wang, G. Synthesis of Fe_2O_3−CNT−Graphene Hybrid Materials with an Open Three-Dimensional Nanostucture for High Capacity Lithium Storage. *Nano Energy* **2013**, *2*, 425−434.
(41) Shamara, Y.; Shamara, N.; Rao, G. V. S.; Chowdari, B. V. R. Nanophase $ZnCo_2O_4$ as a High Performance Anode Materials for Li-Ion Batteries. *Adv. Funct. Mater.* **2007**, *17*, 2855−2861.
(42) Qiao, L.; Wang, X.; Qiao, L.; Sun, X.; Li, X.; Zheng, Y.; He, D. Single Electrospun Porous NiO−ZnO Hybrid Nanofibers as Anode Materials for Advanced Lithium-Ion Batteries. *Nanoscale* **2013**, *5*, 3037−3042.
(43) Wu, Y.; Wei, Y.; Wang, J.; Jiang, K.; Fan, S. Conformal Fe_3O_4 Sheath on Aligned Carbon Nanotube Scaffolds as High-Performance Anodes for Lithium Ion Batteries. *Nano Lett.* **2013**, *13*, 818−823.
(44) Deng, Y. F.; Zhang, Q. M.; Tang, S. D.; Zhang, L. T.; Deng, S. G.; Shi, Z. C.; Chen, G. H. One-Pot Synthesis of $ZnFe_2O_4$/C Hollow Spheres as Superior Anode Materials for Lithium Ion Batteries. *Chem. Commun.* **2011**, *47*, 6828−6830.
(45) Wang, Z. Y.; Luan, D. Y.; Madhavi, S.; Hu, Y.; Lou, X. W. Assembling Carbon-Coated α-Fe_2O_3 Hollow Nanohorns on the CNTs Backbone for Superior Lithium Storage Capability. *Energy Environ. Sci.* **2012**, *5*, 5252−5256.
(46) Yu, W. J.; Hou, P. X.; Li, F.; Liu, C. Improved Electrochemical Performance of Fe_2O_3 Nanoparticles Confined in Carbon Nanotubes. *J. Mater. Chem.* **2012**, *22*, 13756−13763.
(47) Liu, H.; Wang, G.; Wang, J.; Wexler, D. Magnetite/Carbon Core−Shell Nanorods as Anode Materials for Lithium-Ion Batteries. *Electrochem. Commun.* **2008**, *10*, 1879−1882.
(48) Su, D. W.; Kim, H. S.; Kim, W. S.; Wang, G. X. Synthesis of Tunable Porous Hematite (α-Fe_2O_3) for Gas Sensing and Lithium Storage in Lithium Ion Batteries. *Microporous Mesoporous Mater.* **2012**, *149*, 36−45.
(49) Xiao, Z.; Xia, Y.; Ren, Z.; Liu, Z.; Xu, G.; Chao, C.; Li, X.; Shen, G.; Han, G. Facile Synthesis of Single-crystalline Mesoporous α-Fe_2O_3 and Fe_3O_4Nanorods as Anode Materials for Lithium-Ion Batteries. *J. Mater. Chem.* **2012**, *22*, 20566−20573.
(50) Havriliak, S. Jr.; Havriliak, S. J. *Dielectric and Mechanical Relaxation in Materials, Analysis, Interpretation and Application to Polymers*; Hanser Publisher, Cincinnati, OH, 1997.
(51) Jüttner, K. Electrochemical Impedance Spectroscopy (EIS) of Corrosion Processes on Inhomogeneous Surfaces. *Electrochim. Acta* **1990**, *35*, 1501−1508.
(52) Wu, X. L.; Guo, Y. G.; Su, J.; Xiong, J. W.; Zhang, Y. L.; Wan, L. J. Carbon-Nanotube-Decorated Nano-$LiFePO_4$@C Cathode Materials with Superior High-Rate and Low-Temperature Performances for Lithium-Ion Batteries. *Adv. Energy Mater.* **2013**, *3*, 1155−1160.
(53) Wu, M.; Chen, J.; Wang, C.; Wang, F.; Yi, B.; Su, W.; Wei, Z.; Liu, S. Facile Synthesis of Fe_2O_3 Nanotubes/CNTs Composites as High-Performance Anode for Lithium Ion Battery. *Electrochim. Acta* **2014**, *132*, 533−537.